Technical note

Automatic modeling of *pectus excavatum* corrective prosthesis using artificial neural networks

Pedro L. Rodrigues [a,b,c,*], Nuno F. Rodrigues [a,c,d], ACM Pinho [e], Jaime C. Fonseca [b], Jorge Correia-Pinto [a], João L. Vilaça [a,c]

[a] ICVS/3B's—PT Government Associate Laboratory, Braga/Guimarães, Portugal
[b] Algoritmi Center, School of Engineering, University of Minho, Guimarães, Portugal
[c] DIGARC—Polytechnic Institute of Cávado and Ave, Barcelos, Portugal
[d] HASLab/INESC TEC, University of Minho, Braga, Portugal
[e] Mechanical Department, University of Minho, Guimarães, Portugal

ARTICLE INFO

ABSTRACT

Pectus excavatum is the most common deformity of the thorax. Pre-operative diagnosis usually includes Computed Tomography (CT) to successfully employ a thoracic prosthesis for anterior chest wall remodeling. Aiming at the elimination of radiation exposure, this paper presents a novel methodology for the replacement of CT by a 3D laser scanner (radiation-free) for prosthesis modeling.

The complete elimination of CT is based on an accurate determination of ribs position and prosthesis placement region through skin surface points. The developed solution resorts to a normalized and combined outcome of an artificial neural network (ANN) set. Each ANN model was trained with data vectors from 165 male patients and using soft tissue thicknesses (STT) comprising information from the skin and rib cage (automatically determined by image processing algorithms). Tests revealed that ribs position for prosthesis placement and modeling can be estimated with an average error of 5.0 ± 3.6 mm. One also showed that the ANN performance can be improved by introducing a manually determined initial STT value in the ANN normalization procedure (average error of 2.82 ± 0.76 mm). Such error range is well below current prosthesis manual modeling (approximately 11 mm), which can provide a valuable and radiation-free procedure for prosthesis personalization.

© 2014 IPEM. Published by Elsevier Ltd. All rights reserved.

1. Introduction

[-1]*Pectus excavatum* is the most common deformity of the thoracic wall, occurring between 1/400 and 1/1000 births and a male to female ratio of 4:1. It is characterized by a depression in the patient chest, which demands surgical correction in a high percentage of cases [1,2].

A minimally invasive surgical procedure, purposed by Nuss [3], is commonly carried out to remodel the anterior chest wall, by inserting an intrathoracic convex prosthesis (a metal bar) in substernal position [4,5].

In what concerns to prosthesis modeling, only a few works addresses this problem. Lai et al. [6] manually draw the prosthesis shape over ribs position in Computed Tomography (CT) images, achieving accurate prosthesis curvature and length, especially in older patients and females. Vilaça et al. [7,8] developed a novel methodology, composed by mechanical and software models, which automatically model and bend the surgical prosthesis pre-operatively by using (CT) images. The usage of CT for prosthesis modelling is still a controversial issue, since the main driver for *pectus excavatum* surgical correction is cosmesis and the surgery is usually performed in young adolescents (due to their soft cartilages), a population inherently more radiosensitive [9,10]. In order to avoid radiation consequences, Fonseca et al. [11] recently proposed a methodology to reconstruct an axial plane, using 2D ultrasound images, equivalent to a CT-slice. This preliminary study only presents qualitative results, is user dependent and relies on rigid registration between 2D ultrasound images, which may induce additional errors in determining the rib outline.

Regarding the literature pitfalls, this work presents a novel solution aiming at the replacement of the CT by a radiation-free 3D laser scanner to automatically model the surgical prosthesis. Considering the ability of artificial neural networks (ANN's) to approximate

* Corresponding author at: Life and Health Sciences Research Institute (ICVS), School of Health Sciences Campus, ICVS/3B's—PT Government Associate Laboratory, University of Minho, 4710-057 Braga, Portugal. Tel.: +351 253604881; fax: +351 253 604 847.
E-mail address: pedrorodrigues@ecsaude.uminho.pt (P.L. Rodrigues).
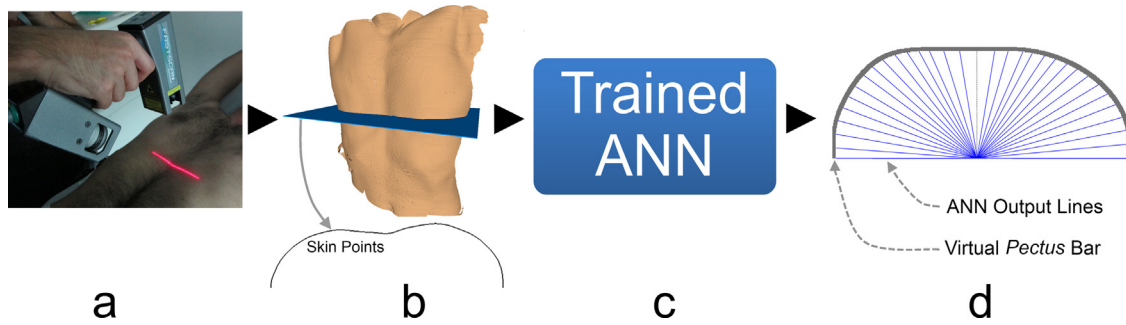
Fig. 1. Overview of the main steps to automatic model/bend the thoracic prosthesis using 3D scan data. (For interpretation of the references to color in this figure legend, the reader is referred to the web version of this article.)

non-linear functions, these computational structures were chosen to infer the ribs position from the 3D model of the patient chest surface acquired by the 3D scanner.

2. Methods

Fig. 1 provides an overview of the proposed new method, presenting the main steps for prosthesis modeling:

(a) Acquisition and reconstruction of the full anterior chest wall surface of the patient, using the 3D laser scanner (Fig. 1a).
(b) Determination of the skin line that transversely passes though the greatest sternum depression point (Fig. 1b). This set of points determine the position in the patient's skin surface under which the prosthesis bar is implanted.
(c) ANN software module that receives the set of skin points calculated in the previous step and computes the necessary set of lines (blue lines in Fig. 1c) for *pectus* prosthesis modeling (Fig. 1d) [7,8].

All the applied methods for the acquisition of the ANN training vectors were implemented using C++ with VTK (The Visualization ToolKit) and ITK (Segmentation & Registration Toolkit) support, while the ANN training procedure was implemented and tested using the neural network toolbox from MATLAB.

2.1. 3D Chest wall surface reconstruction

The patient 3D chest wall surface reconstruction begins by repeatedly swiping the laser scan (from FastSCAN Polhemus Liberty) over the anterior patient chest. An electromagnetic tracking system is used to track the scanner wand location in the 3D space. Equipment specifications determine that acquisition resolution depends on wand-object range, guaranteeing a 0.5 mm resolution at 200 mm range and improved resolutions (as low as 0.1 mm) for smaller ranges. Considering this, all scans were performed bellow 200 mm wand-object range.

The reconstruction of the thoracic wall mesh, from the acquired point cloud (Fig. 2a), was based on Hoppe et al. work [12], which comprehends an algorithm that determines the zero set of an estimated signed distance function, and is capable of automatically
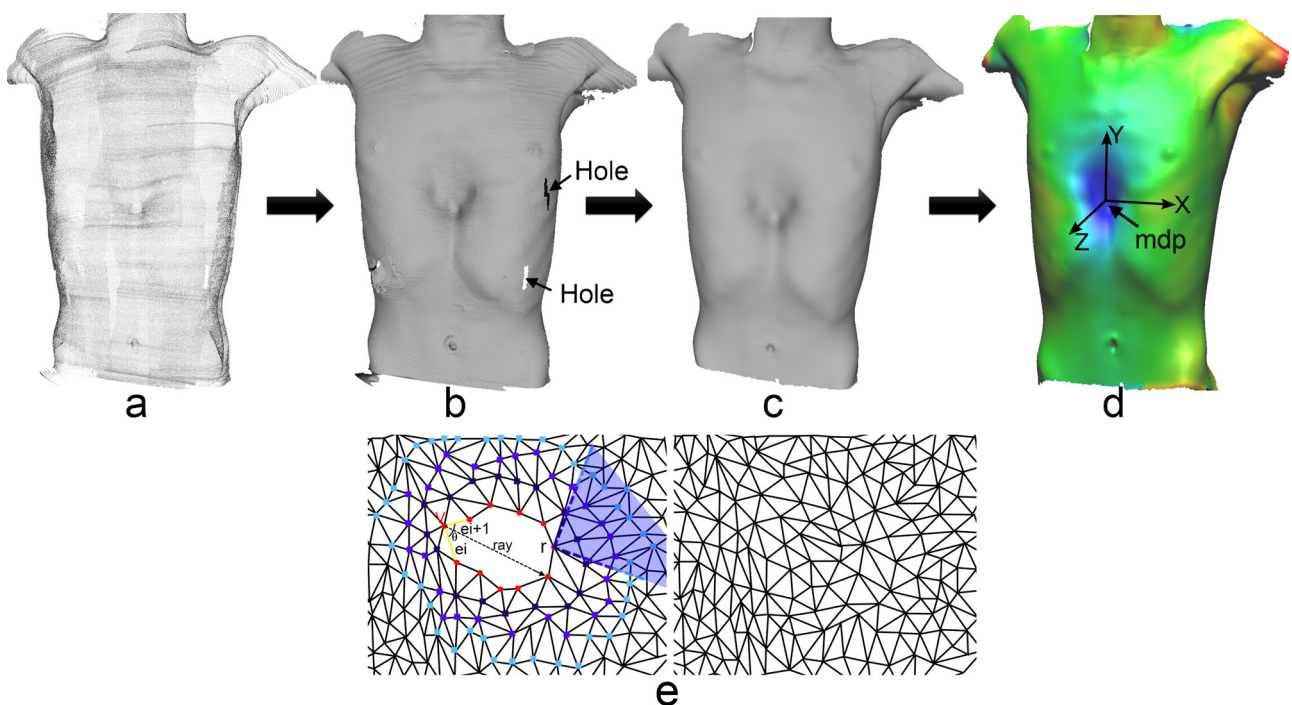
Fig. 2. Overview of the chest wall surface reconstruction: (a) unorganized point cloud; (b) chest wall surface mesh with holes; (c) smoothed surface mesh without holes; (d) color map showing distances along Z axis and the maximum depression point; (e) left: schematic of the algorithm for filling a hole in a surface triangle mesh; right: surface without holes after the filling holes method. (For interpretation of the references to color in this figure legend, the reader is referred to the web version of this article.)

Table 1
Automatic algorithm for mesh hole filling.

Input: Mesh with holes
Output: Smoothed mesh surface without holes
% *Data Structures*
Vertice:: (int, int, int) *% A vertices is defined with 3 integers*
Edges:: (vertex, vertex) *% An edge is defined with 2 vertices*
Triangle:: (Edge, Edge, Edge) *% A triangle is defined with 3 edges*
Mesh:: [Triangle] *% A mesh is defined with a list of triangles*
% *Variables*
surfaceMesh: Mesh *% Thoracic wall mesh*
singleEdges: [Edge] *% List of all edges that shares only 1 triangle—Mesh hole*
edgeClosures: [[Edge]] *% List of list of edges for each holes in the surface mesh*
edgeClosuresVertices: [[Vertex]] *% List of list of vertices for each hole in the surface mesh*
holeRing: [[L][Vertex]] *% List of list of vertices that defines a ring of edges around the hole at level L (Fig. 2e)—Level 1—dark blue square points; Level 2—blue square points; Level 3—light blue square points)*
ray: [[Vertex]] *% List of list of rays*
nurb: Mesh *% Final Mesh that fills the hole*
%Processing
singleEdges ← GetSingleEdges(surfaceMesh) *% Detect all the holes in the given triangular mesh surfaceMesh by identifying all edges that are shared by a single triangle*
edgeClosures ← GetEdgeClosures(singleEdges) *% Label different edges as belonging to a different surface mesh holes, by automatically searching the subsets of edges that are connected to each other and form a closed path.*
edgeClosuresVertices ← GetVertices(edgeClosures) *% Get vertices from each edgeClosure*
For each Vertice v in edgeClosuresVertices
  (Edge_i, Edge_iplus) ← GetAdjacentEdges(v) *%(Fig. 2e)—ei and ei + 1*
  Double ang ← CalculateAngle(Edge_i, Edge_iplus) *% Calculate the angle (Fig. 2e)—angle θ between two adjacent boundary edges(Edge_i and Edge_iplus)*
  ray[v] ← CreateRay(v, θ/2) *% Calculate a ray with starting point in a hole vertex V and direction define by the θ/2 between the two edges that shares V (ray in Fig. 2e)*
  GetLevelRing(holeRing, v) *% Calculate points at the different three levels of vertices around the hole (blue squares in Fig. 2e)*
End
  nurb ← CreateNURB[*](ray, holeRing) *% Estimate the missing mesh surface through the calculation of Non-Uniform Rational B-Splines from previously calculated data*
  nurb ← LaplacianSmooth(nurb) *% Laplacian smooth method to reduce the shrinking effect*

[*] *CreateNURB* function implements a NURB curve [8] defined as $C(t) = \left(\sum_{i=0}^{n} N_{i,p}(t)w_iP_i\right) / \left(\sum_{i=0}^{n} N_{i,p}(t)w_i\right)$ where $p = 3$ is the surface order, $N_{i,p}(t)$ is the B-Spline function, W_i is the weight for curve smoothness and P_i are the control points calculated from the starting and end point of the ray and its ring neighbors.

Table 2
Summary of anatomical STT characterization of all patients.

STT Differences according to patient side		
Measured area	Left	Right
Breasts	9.90 ± 3.6	11.0 ± 3.2
Most lateral areas	22.2 ± 6.23	23.8 ± 7.1
Other thoracic wall angles	11.9 ± 6.9[*]	12.3 ± 6.7[*]

[*] The coefficient of variation among all patients was 0.37.

the definition of ANN in terms of topology and training algorithms (Section 2.2.2).

2.2.1. ANN training vectors

2.2.1.1. Population data. ANN's models were trained and validated with information acquired from thorax CT scans of 165 different patients. Test data consists of information acquired with the laser scanner from 20 other patients. These have also been subject to CT examination to serve as ground truth data of the ribs structures.

Each CT slice has 512×512 pixel, with a slice thickness of 3 mm. The age of all patients ranged from 5 to 18 years (mean of 13.55 ± 3.42). Female patients were not considered in this study because of the impossibility of correlating the breasts with the shape of the ribs. Regarding STTs characterization Table 2 shows the STT differences in different areas along the thoracic wall.

2.2.1.2. Axial plane prosthesis placement. The employed methodology starts with the automatic calculation of the axial plane with the greatest sternum depression (number 4, Fig. 3a and b). To this extent, the noise corrupting the CT image is firstly reduced by smoothing the image with a Gaussian filter ($\sigma = 2$ pixel). Then, a sigmoid non-linear filter mapped the image intensities into a new range. The output pixel I' was given by $I' = (I_{Max} - I_{Min}) \times (1/(1 + \exp(-((I - \beta)/\alpha))))$ where I is the input pixel intensity, I_{Max} (=3000) and I_{Min} (=0) output maximum and minimum intensities, α (=400) is intensity range width and β (=1500) is the intensity around which the range is centered. These values were determined experimentally in order to enhance the bones structures. These were finally segmented using a threshold method, which level was automatically calculated as the one maximizing the total entropy E_T of the binary output: $E_T = E_B(i) + E_O(i)$, where $E_O(i)$ is the total object entropy and $E_B(i)$ is the total background entropy. The sternum structure was finally isolated as the most anterior structure (Fig. 3a).

The inferior sternum region with highest depression, which corresponds to the desired CT slice to place the prosthesis, was determined using a ray-pixel intersection method that computes the minimum distances between the coronal plane (Tp, Fig. 3b) parallel to the chest wall and the sternum (Ts, Fig. 3b).

Although the xiphoid process (number 2, Fig. 3a) showed the greatest depression values, this small structure was not considered due to its low ossification and inability to support the prosthesis during two/three years of implantation [13].
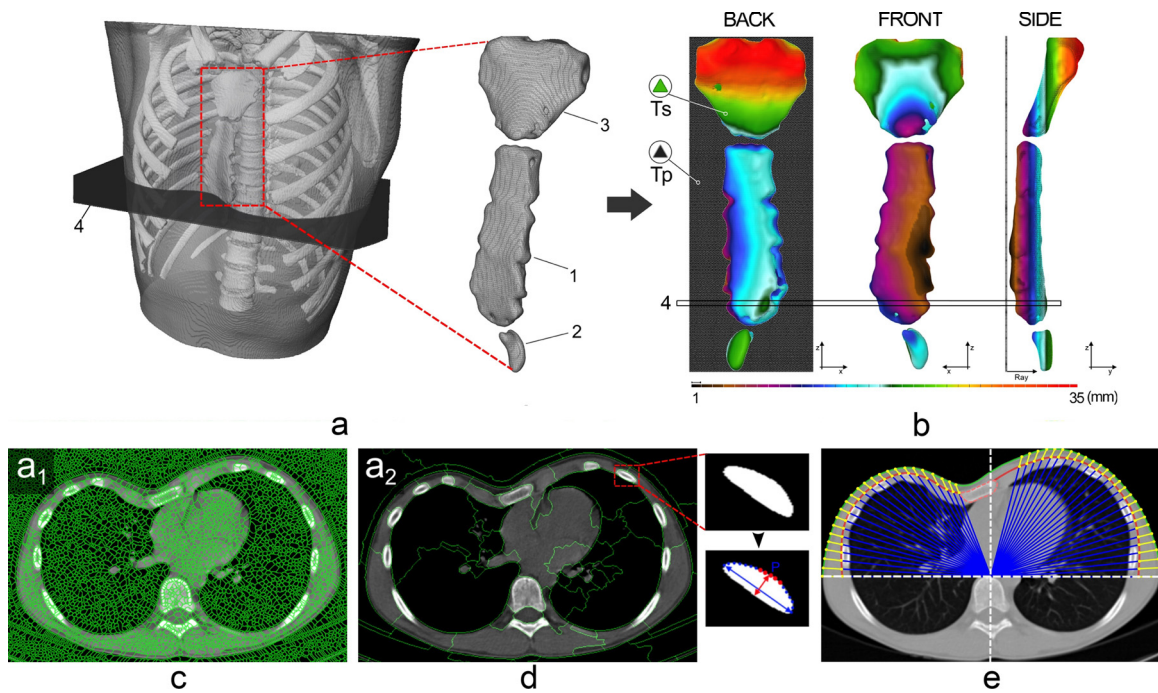
2.2.1.3. STT calculation.
2.2.1.3.1. Bone and skin segmentation. The calculation of the STT, for the ANN training procedure, was accomplished by determining the ribs external outline (red polynomials in Fig. 3e) and skin points (green points in Fig. 3e) in CT images.

The skin points were segmented from the non-linear filter outcome, using the Otsu threshold method. All skin pixels were selected by vertically and horizontally tracking the first pixels in the binary image object.

On the other hand, bone structures where segmented using a region-based methodology, previously developed by the authors in volumetric CT datasets [14,15]. The process uses the gradient

---

inferring the topological type of the surface, including the presence of boundary curves.

The resulting triangular mesh (Fig. 2b) of the patient thorax often contains small surface holes due to inappropriate conditions during scan acquisition, namely patient movements and occlusions. Even though the mesh holes do not represent a significant problem for the calculation of the transversal chest line to place the prosthesis, it does influence the validation of the 3D thorax scan quality, in particular for its comparison with CT scans. Therefore, one has developed an automatic process for detecting and filling the mesh holes (Table 1). NURBS were chosen due to their smoothing properties, finer shape control, flexibility to design large variety of shapes and good overall curve.

The main purpose of the thorax reconstruction is to identify an axial slice that passes through the maximum depression point (MDP) (skin points line in Fig. 2b). The MDP is determined by considering the maximum value of the distance map along Oz (Fig. 2c and d) at the mesh center region.

2.2. ANN software module development

The ANN model development comprehended 2 main phases, namely the acquisition of the training vectors (Section 2.2.1), and

Fig. 3. Overview of the different steps to automatically determine the region of the greatest sternum depression: (a) 3D sternum structure: 1-sternum, 2-xiphoid process and 3-manubrium; (b) ray intersection results and the greatest sternum depression slice (number 4); ((c) and (d)) representation of different image partitioning for bone segmentation; (d) also shows a schematic how the control points were determined to define ribs external contour line; (e) representation of different substructures segmented in a CT axial slice: bone segmentation at surgical prosthesis location (polynomials in red); skin segmentation; representation of lines between the central anatomical point and the patient ribs and skin surface used for ANN training. (For interpretation of the references to color in this figure legend, the reader is referred to the web version of this article.)

magnitude of the non-linear filter and the minimum description length algorithm to create an image partitioning of different levels (Fig. 3c and d).

This outcome was used to calculate the coronal and sagittal planes that define the regions for prosthesis placement and a reference point for all the lines used to acquire the STT (Fig. 3e).

Although an automatic segmentation methodology to accelerate STT identification was used, the final results were manually validated in order to assure sound training vectors.

2.2.1.3.2. STT training vectors. After bone segmentation, two polynomials were calculated by a Monotone cubic Hermite interpolation spline [16], one to delineate the external contour line of the left ribs and another to delineate the right ribs (red line in Fig. 3e).

The STT external to the ribs was determined through different lines which slope was incremented with from $0°$ to $80°$ (step of $1°$), and decremented from $180°$ to $100°$ (step of $1°$), on the right and left sides of the patient, respectively (blue and yellow lines, Fig. 3e). The reference point for all these lines was the intersection between the coronal and median planes. These polynomials allow the STT determination in all regions where the prosthesis is placed, instead of only considering the ribs locations.

The STT computational representation in the training vectors is defined by 2 sets of line segments: the first set is defined by the distances in millimeters between the reference point and the patient ribs (blue lines in Fig. 3e), while the second set corresponds to the distances between the same reference point and the chest surface (blue plus yellow lines in Fig. 3e).

2.2.2. ANN topology, training and ensemble normalization

Considering the ability to approximate non-linear functions, two different networks topologies were used for predicting the external ribs outline: FNN's (feed-forward neural networks) and CNN's (cascade-forward neural networks—includes a weight connection from the input to each layer and a connection from each layer to the successive layers) [17].

During training, the weights and biases of the network (randomly initialized) were iteratively adjusted to maximize the network performance function that measures the mean squared error between the ANN output vector and the ANN target vector.

Four different training algorithms were used to adjust the weights and biases of the ANN models. Three of these training algorithms are conjugate gradient algorithms, namely Scaled Conjugate Gradient (SCG), Levenberg–Marquardt (LM) and Resilient Back propagation (RP), while the fourth is a One Step Secant (OSS) algorithm named Quasi–Newton algorithm [18–21].

Conjugate gradient algorithms start by moving the network weights and biases along the negative gradient of the performance function based on a back propagation technique. These algorithms were chosen because:

(a) LM is a known algorithm with reduced processing time for convergence, accurate results and lower mean square errors for problems with a small number of network weights;
(b) SCG and RP have also been extensively used over a wide variety of problems and medical applications [22–24], particularly for networks with a large number of weights. These are almost as fast as the LM algorithm on function approximation problems and even faster for large networks;
(c) OSS Newton's method often converges faster than conjugate gradient methods and requires less storage and computation per epoch, making it useful to approximate non-linear relationships.

The optimal ANN model was found by a systematic and repetitive process during which the number of hidden layers (between 1 and 4) with different number of neurons (between 15 and 75

Table 3
CC scores between different ANN with different training algorithms, topologies, neurons and hidden layers.

Training algorithm	ANN topology	One hidden layer					Two hidden layer				
		15	25	45	55	75	15	25	45	55	75
SCG	FNN	0.78 ± 0.12	0.90 ± 0.07	0.87 ± 0.02	0.81 ± 0.11	0.84 ± 0.05	0.69 ± 0.28	0.99 ± 0.16	0.93 ± 0.15	0.92 ± 0.25	0.88 ± 0.21
	CNN	0.69 ± 0.24	0.86 ± 0.09	0.97 ± 1.47	0.93 ± 1.77	0.84 ± 0.08	0.79 ± 0.11	0.87 ± 0.07	0.85 ± 0.06	0.80 ± 0.21	0.82 ± 0.15
LM	FNN	0.75 ± 1.9	0.86 ± 0.04	0.92 ± 0.45	0.87 ± 1.8	0.72 ± 2.12	0.83 ± 1.27	0.96 ± 0.17	0.93 ± 0.37	0.91 ± 0.87	0.91 ± 1.44
	CNN	0.66 ± 2.8	0.90 ± 0.12	0.93 ± 0.23	0.89 ± 1.35	0.78 ± 1.94	0.81 ± 2.7	0.95 ± 1.2	0.92 ± 0.57	0.90 ± 1.45	0.88 ± 4.2
RP	FNN	0.75 ± 2.67	0.89 ± 0.06	0.94 ± 0.02	0.89 ± 0.18	0.92 ± 2.56	0.88 ± 1.20	0.97 ± 0.89	0.91 ± 0.06	0.92 ± 0.37	0.79 ± 1.10
	CNN	0.77 ± 2.4	0.86 ± 0.70	0.94 ± 1.03	0.92 ± 1.57	0.89 ± 0.91	0.89 ± 1.25	0.97 ± 0.17	0.91 ± 0.68	0.91 ± 0.43	0.81 ± 2.44
OSS	FNN	0.53 ± 2.65	0.83 ± 1.76	0.80 ± 2.10	0.75 ± 4.7	0.69 ± 2.28	0.64 ± 1.52	0.78 ± 1.98	0.74 ± 2.27	0.60 ± 4.9	0.47 ± 2.20
	CNN	0.68 ± 6.02	0.72 ± 0.21	0.65 ± 2.6	0.71 ± 5.55	0.78 ± 6.02	0.71 ± 5.4	0.81 ± 5.8	0.78 ± 7.2	0.65 ± 0.10	0.54 ± 2.51

sigmoid neurons) were changed for CNN and FNN topologies and training algorithms.

The training procedure was performed 15 times for each network configuration until one of the following parameters was achieved: (1) number of epochs was higher than 1000; (2) minimum error gradient lower than $1 \times 10e-5$; (3) maximum number of iterations on which the gradient error increases was lower than 10—avoiding overfitting situations; (4) small learning rate of 0.15.

In the end, the ANN performance was evaluated through a statistical regression analysis, measuring the correlation coefficient (CC) between the output and target vectors (strong correlation when CC > 0.90).

Instead of taking into account only one network output to predict the ribs external contour, an ensemble solution from a set S_N of ANN models (with $i = 1,2,\ldots,N$ with N being the total number models) with a CC score higher than 0.92 through the following steps:

(1) Each ANN model M_i (with $i = 1,2,\ldots,N$ with N being the total number of ANN models in the set S_N) predicts the distances between the reference points and the ribs external outline along the thoracic wall for each patient of the test data.
(2) When M_i did not converge to a reliable result (convergence evaluated taking into account the entropy, average, minimum and maximum values of the network outcomes), M_i was discarded from S_N.
(3) The harmonic mean of the remaining networks M_i in S_N were input to a normalization procedure that computes the final ribs external contour by adjusting the harmonic mean values whenever:
  (a) The difference between the STT of the line with slope i and the one of a line with slope $i-1$ was higher than 4 mm.
  (b) The length of the line from the reference point to the skin was smaller than the distance determined with the ANN (rib point).
  (c) For each case described in (a) and (b) a new length is determined in accordance with a weighted mean of the three previous lengths.

Initially all ANN models with CC > 0.92 ($N > 100$) were used to predict the ribs outline according to the previous steps. However, since this solution required a significant computational effort, one decided to remove neural networks with lower CC, while studying its repercussions in the final result. The optimum value of $N = 30$ ANN models assured the best compromise between performance and accuracy when predicting the ribs outline, with no statically differences when compared to using all ANN models.

Given that the computed STT in a certain angle is influenced by its neighboring values, the accuracy and reliability of the results computed was also evaluated when using a manually determined initial STT values after the ANN normalization procedure (i.e. for points in 0° and 180° calculated from the CT axial slice).

3. Results

Depending on the number of active neurons and hidden layers, ANN usually took 7 to 85 s to be fitted using an Intel Core i7 Q740 1.73 GHz computer. Table 3 shows the CC scores (average and standard deviation) for different ANN models with various configurations of number of neurons, hidden layers, training algorithms and topologies.

Independently of the ANN architecture, fewer neurons in the hidden layer (25–45 neurons) performed better than a higher number of neurons (>75 neurons). With a higher number of neurons the ANN object overfits the training data instead of generalizing the input and target relationships.

Best results were obtained with the SCG (Table 3) training algorithm and FNN topology, therefore, only those ANN objects will be discussed. The closest results were gathered using the RP training algorithm. From Table 3, conjugate gradient backpropagation algorithms shown to be the best with higher CC scores. Although the OSS was the training algorithm with fastest convergence, it also shows lower CC scores.

Fig. 4 shows the STT error when (1) using the manual modelling template that copies the skin points (Fig. 4a and b); (2) ANN outcome without normalization (Fig. 4c and d); (3) ANN with normalization (Fig. 4e and f); (4) ANN with normalization and first points (Fig. 4g and h).

As shown in Fig. 4, the highest errors for ideal prosthesis modeling are with the skin points. For both patient sides, the error is always higher than 5 mm. Apart from ANN output, highly statistical significance ($p < 0.001$) was always found between ANN outcome and skin points.

Table 4 shows the average STT error for all 20 patients when using the skin points, ANN without normalization and input point, ANN with normalization algorithm and ANN with normalization algorithm and input points.

Fig. 5 illustrates some examples of the ANN output overlapped by the bone ground truth outline obtained from CT images.

Table 4
STT average and standard deviation errors for prosthesis modeling according to different input data.

STT error for prosthesis modeling according to the patient side (mm)		
Input model data	Left	Right
Skin points	11.34 ± 3.99	12.07 ± 4.03[*]
ANN	7.04 ± 5.29	6.60 ± 6.20[#]
ANN + norm	4.92 ± 3.23	5.10 ± 3.98[&]
ANN + norm + input points	2.98 ± 0.88	2.67 ± 0.63

[*] High significant differences ($p < 0.001$) with other input models for both patient sides.

[#] Significant differences ($p < 0.05$) for the left patient side and non-significant differences ($p > 0.05$) for the right side, when compared to ANN + norm. High significant differences ($p < 0.001$) with ANN + norm + input points for both patient sides.

[&] Statistical differences ($p < 0.01$) with ANN + norm + input points for both patient sides.
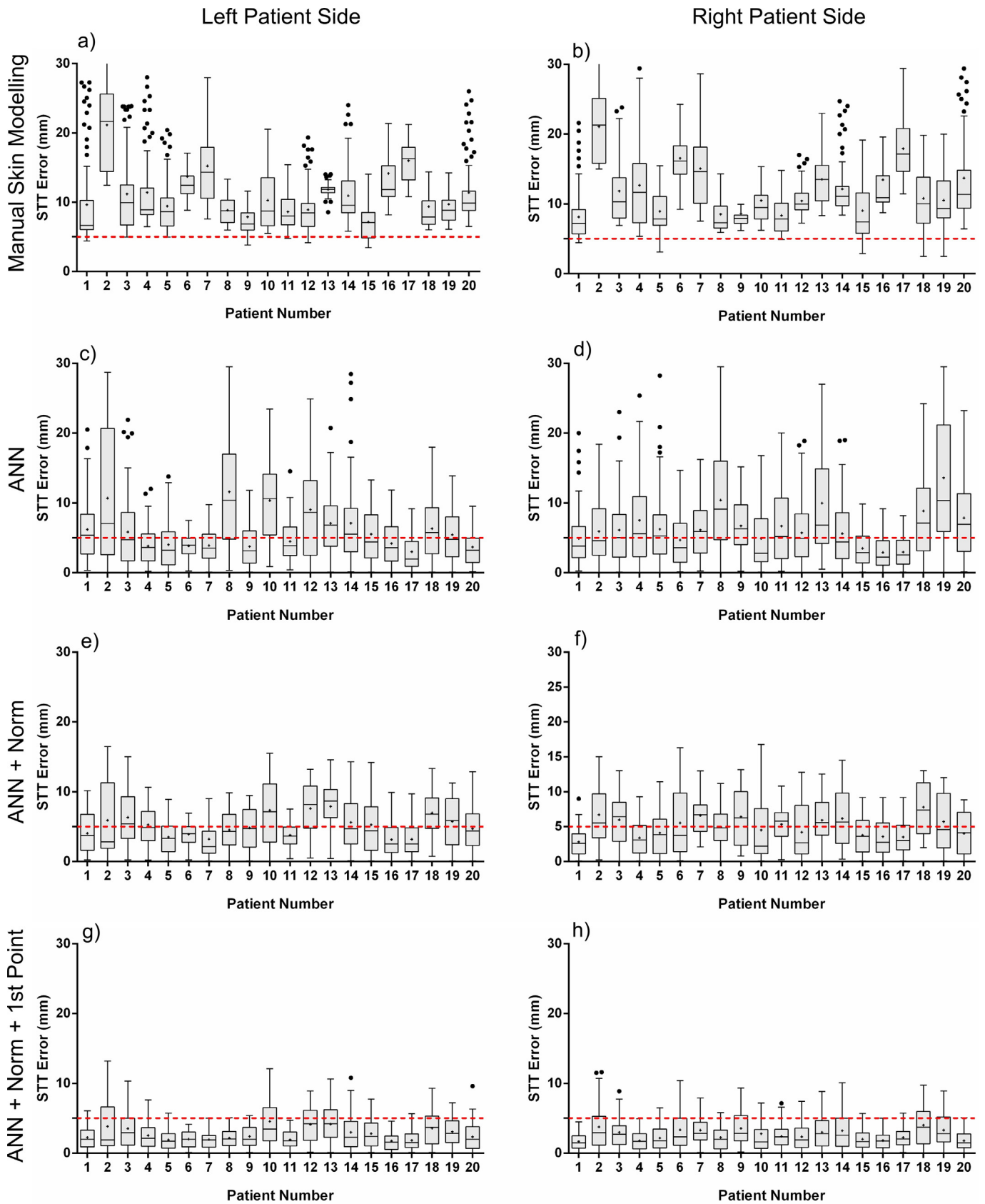
Fig. 4. Boxplots of the STT error according to 30 ANN topologies to predict ribs position in 20 patient test data. The boxplots have ends at one and three quartiles (Q1 and Q3). The horizontal line in the box shows the median of data. The farthest points that are not outliers (i.e. that are within 1.5 times the interquartile range of Q1 and Q3) are shown as sphere points. The mean errors are shown by crosses within the box. The red line shows the 5 mm error.
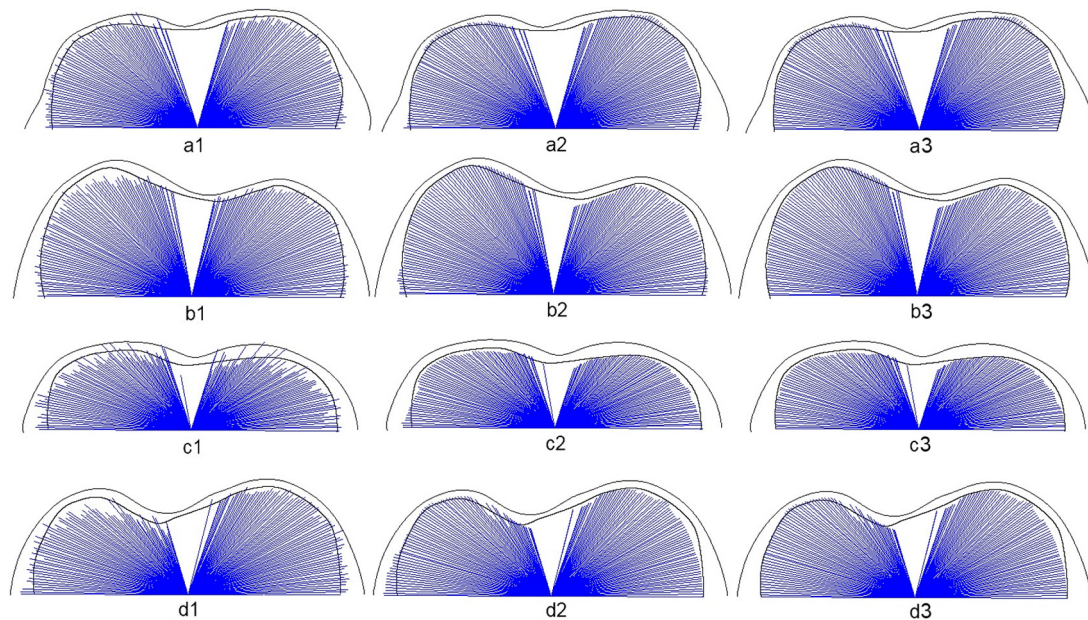
Fig. 5. Illustration of different ANN results (blue lines) when using the ANN without normalization and input points (a1, b1, c1 and d1), ANN with normalization (a2, b2, c2 and d2) and ANN with normalization and initial input points (a3, b3, c3 and d3). (For interpretation of the references to color in this figure legend, the reader is referred to the web version of this article.)

4. Discussion

The study of the STT showed that symmetric or asymmetric patients have always asymmetric variations in STT. The necessity of modeling and bending the thoracic prosthesis using ribs position and dimension is of outmost importance, in particular when taking into account the asymmetry of each patient, instead of using a template that only copies the chest wall curvature [25].

Conducted tests showed that ribs position can be estimated with an average error of 4.9 ± 3.23 mm and 5.1 ± 3.98 mm for the left and right side of the patient using ANN with a normalization procedure.

The highest errors in this study were found in lower (0–15°) and higher angles (65–80°) due to patient anatomic variability in these areas, making ANN not always able to converge to a desirable function. Therefore, the ANN outcome was improved by introducing a manually determined initial STT value, which can be acquired in future by a simple ultrasound procedure, without involving any radiation exposure. This allowed the average STT error to be further reduced to 2.98 ± 0.88 mm and 2.67 ± 0.63 mm for the left and right side of the patient.

Although, with limited user input, this methodology will no longer fulfill the fully automated requirement, it increases the accuracy and suitability while decreasing the procedure uncertainty. The main associated problems were due to physical characteristics, namely morphology deformity, degree of asymmetry and patient age.

However, this last methodology demands further evaluation regarding its clinical applicability. After further tests one found that the average error tends to increase from 2.82 mm to 2.95, 3.21, 3.33 and 3.44 mm when the input points where shifted from the ideal position in 1, 2, 3 and 4 mm. Although this offset error may be dependent on the physician expertise or imagiology system, one offset error up to 5 mm still yields to better results when compared to manual modeling or ANN itself without a first point.

The overall magnitude of the errors obtained allows one to discharge them, as the current prosthesis manual modeling error (Fig. 4a and b) is commonly higher than 10 mm, due to the high STT in some patients.

Although magnetic resonance (MR) and ultrasound (US) are also radiation-free options, they also comprise some shortcomings. MR is more expensive than the laser scan and unaffordable for some clinics. On the other hand, US does not provide direct information regarding the entire rib cage, which significantly limits the automatic modeling and ribs segmentation for prosthesis placement. However, the US can be used to check if the ANN's outcome is reliable in some lateral positions.

5. Conclusion

This study explores the substitution of CT by 3D laser scanning in the treatment of *pectus excavatum*. The final result of this work is a software capable of computing personalized shapes of *pectus excavatum* prosthesis, based on 3D scan from the patients' thorax. The results obtained show that 3D scan technology, combined with state of the art knowledge and techniques in image processing and intelligent algorithms, represents a valid alternative for prosthesis modeling in *pectus excavatum* surgical correction. One can also speculate the applicability of such an approach to the diagnosis itself for *pectus excavatum*.

In spite of the promising results, several research paths for the improvement of the developed process should be investigated. In particular, one should explore the impact of an increased number of patients to train the ANN, use classified groups of patients according to the different morphological types of *pectus excavatum*, and investigate how the process could be extended to female patients.

Ethical approval

Not required.

Conflict of interest statement

The CT images for the 185 patients were acquired at São João Hospital, Porto, Portugal and Hospital of Braga, Portugal, according to the ethical review board of the University of Minho.

References

[1] Kim DH, Hwang JJ, Lee MK, Lee DY, Paik HC. Analysis of the Nuss procedure for *pectus excavatum* in different age groups. Ann Thorac Surg 2005;80:1073–7.

[2] Krasopoulos G, Dusmet M, Ladas G, Goldstraw P. Nuss procedure improves the quality of life in young male adults with *pectus excavatum* deformity. Eur J Cardiothorac Surg 2006;29:1–5.

[3] Nuss D, Kelly RE, Croitoru DP, Katz ME. A 10-year review of a minimally invasive technique for the correction of *pectus excavatum*. J Pediatr Surg 1998;33:545–52.

[4] Wang W-D, Shi Y-K, Wang H, Yin L-N. Research on biomechanical model of children with *pectus excavatum*. Second international conference on biomedical engineering and informatics 2009 (BMEI'09) 2009:1–4.

[5] Park HJ, Lee SY, Lee CS, Youm W, Lee KR. The Nuss procedure for *pectus excavatum*: evolution of techniques and early results on 322 patients. Ann Thorac Surg 2004;77:289–95.

[6] Lai J-Y, Wang C-J, Chang P-Y. The measurement and designation of the pectus bar by computed tomography. J Pediatr Surg 2009;44:2287–90.

[7] Vilaça JL, Pinho A, Correia-Pinto J, Fonseca J, Peixinho N. System for automatic and personalized modelling/bending of surgical prosthesis for correction of *pectus excavatum* based on pre-surgical imagiology information. In: Patent, WO2009/035358; 2009.

[8] Vilaça JL, Henriques-Coelho T, Soares TR, Fonseca J, Pinho A, Rodrigues PL, et al. Automatic pre-bended customized prosthesis for *pectus excavatum* minimal invasive surgery correction. Surg Innov 2013.

[9] Hollingsworth C, Frush DP, Cross M, Lucaya J, Helical CT. of the body: a survey of techniques used for pediatric patients. AJR: Am J Roentgenol 2003;180: 401–6.

[10] Mao Y-Z, Tang S-T, Wang Y, Tong Q-S, Ruan Q-L. Nuss operation for *pectus excavatum*: a single-institution experience. World J Pediatr 2009;5:292–5.

[11] Fonseca JG, Moreira AHJ, Rodrigues PL, Fonseca JC, Pinho ACM, Correia-Pinto J, et al. Thoracic wall reconstruction using ultrasound images to model/bend the thoracic prosthesis for correction of *pectus excavatum*. SPIE Medical Imaging 2012, 83200L-L-11.

[12] Hoppe H, Derose T, Duchamp T, Mcdonald J, Stuetzle W. Surface reconstruction from unorganized points. Comput Graphics 1992;26:71–8.

[13] Alexander AF, Nury MS, William AA, Karen EA. Anatomical, histologic, and genetic characteristics of congenital chest wall deformities. Semin Thorac Cardiovasc Surg 2009;21:44–57.

[14] Rodrigues PL, Moreira AHJ, Fonseca JC, Pinho ACM, Rodrigues NF, Vilaça JL. A region-based algorithm for automatic bone segmentation in volumetric CT. NOVA Publishers; 2012.

[15] Rodrigues PL, Vilaça JL, Fonseca JC. An image processing application for liver tumour segmentation. First Portuguese meeting (ENBENG) Lisbon 2011:1–6.

[16] Fritsch FN, Carlson RE. Monotone piecewise cubic interpolation. SIAM J Numer Anal 1980;17:238–46.

[17] Goyal S, Goyal GK. Cascade and feedforward backpropagation artificial neural network models for prediction of sensory quality of instant coffee flavoured sterilized drink. Can J Artif Intell Mach Learn Pattern Recognit 2011:2.

[18] Møller MF. A scaled conjugate gradient algorithm for fast supervised learning. Neural Networks 1993;6:525–33.

[19] Hagan MT, Menhaj MB. Training feedforward networks with the Marquardt algorithm. IEEE Trans Neural Networks 1994;5:989–93.

[20] Riedmiller.Proceedings of the IEEE international conference on neural networks (ICNN). 1993. p. 586–91.

[21] Battiti R. First- and second-order methods for learning: between steepest descent and Newton's method. Neural Comput 1992;4:141–66.

[22] Ceylan R, Ozbay Y, Karlik B. A novel approach for classification of ECG arrhythmias: type-2 fuzzy clustering neural network. Expert Syst Appl 2009;36:6721–6.

[23] Güler İ, Übeyli ED. Implementing wavelet/probabilistic neural networks for Doppler ultrasound blood flow signals. Expert Syst Appl 2007;33:162–70.

[24] Xie H-B, Zheng Y-P, Guo J-Y, Chen X, Shi J. Estimation of wrist angle from sonomyography using support vector machine and artificial neural network models. Med Eng Phys 2009;31:384–91.

[25] Rodrigues PL, Direito-Santos B, Moreira AH, Fonseca JC, Pinho AC, Rodrigues NF, et al. Variations of the soft tissue thicknesses external to the ribs in *pectus excavatum* patients. J Pediatr Surg 2013;48:1878–86.